Electronic Supplementary Information

A gradient Sn^{4+}@Sn^{2+} core@shell structure induced by strong metal oxide-support interaction for enhanced CO_2 electroreduction

Shun Zhang [a,c], Juan Wang [a], Jie Wang [a], Kai-Yao Wang [a], Meiting Zhao[d], Linlin Zhang [a,b]*, and Cheng Wang [a]

[a] Tianjin Key Laboratory of Advanced Functional Porous Materials and Center for Electron Microscopy, Institute for New Energy Materials & Low-Carbon Technologies, School of Materials Science and Engineering, Tianjin University of Technology, Tianjin 300384, China

[b] CAS Key Laboratory of Design and Assembly of Functional Nanostructures, Fujian Key Laboratory of Nanomaterials, Fujian Institute of Research on the Structure of Matter, Chinese Academy of Sciences, Fuzhou 350002, China

[c] Wenzhou Institute, University of Chinese Academy of Sciences, Wenzhou 325000, People's Republic of China

[d] Institute of Molecular Aggregation Science, Tianjin University, Tianjin 300072, China

*To whom correspondence should be addressed

E-mail: zhanglinlin_cn@126.com

Table of content

1. Supplementary experiments

2. Supplementary figures and tables

1. Supplementary experiments

1.1 Preparation of g-C_3N_4 nanosheets

g-C_3N_4 nanosheets were synthesized according to a reported method with slight modifications. [1] Typically, 6 g of urea was placed in crucible with a lid and annealed at 550 ^oC for 2 h with a ramping rate of 1 ^oC min^{-1} under the flow of N_2 in a tube furnace. After cooling down to the room temperature, light yellow powders of g-C_3N_4 nanosheets were obtained.

1.2 Preparation of GO nanosheets

Graphite oxide (GO) nanosheets were fabricated according to a modified Hummer' method. [2] Firstly, an aqueous solution containing 180 mL of H_2SO_4 and 20 mL of H_3PO_4 was added to the powders of $KMnO_4$ (9.0 g) and graphite (1.5 g). The mixture was then stirred for 12 h. After cooling to room temperature, the suspension was mixed with an aqueous solution of H_2O_2 (30%) and a certain amount of ice. Then, the mixtures were centrifuged for 20 min with a rotation rate of 2000 rpm before being washed with water, concentrated hydrochloric acid solution and anhydrous ethyl ether at least twice. Finally, brownish GO nanosheets were collected after filtration using a polytetra fluoroethylene (PTFE) membrane with a pore size of 0.45 μm, followed by vacuum drying overnight at the ambient temperature.

2. Supplementary figures and tables

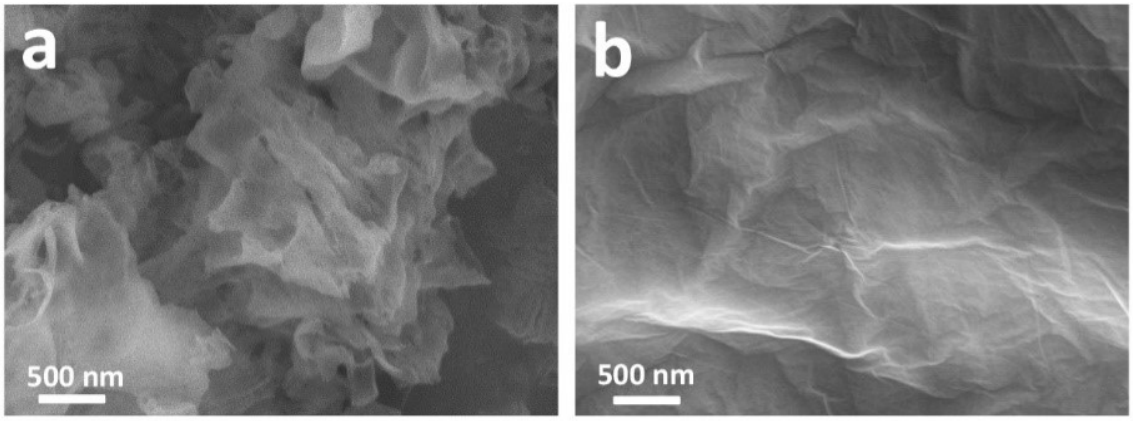

Fig. S1. SEM images of g-C_3N_4 (a) and GO (b) nanosheets.

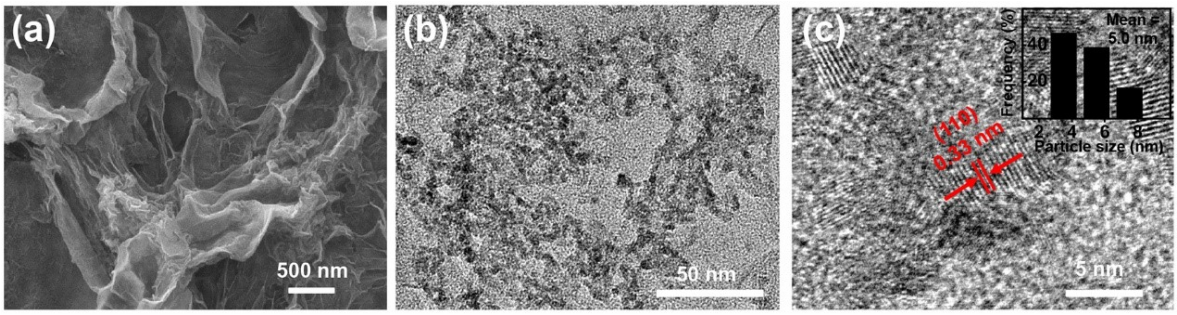

Fig. S2. SEM (a), TEM (b) and HRTEM (c) images of SnO_2/rGO

Fig. S1 and **S2** showed the morphologies and microstructures of g-C_3N_4, graphene oxide (GO) and SnO_2/rGO, respectively. Obviously, the surface of GO was slightly smoother than that of g-C_3N_4. During the hydrothermal process, GO was thermally converted to the reduced graphene oxide (rGO). Meanwhile, SnO_2 nanoparticles were grown on the rGO support homogeneously and densely via a hydrolysis-condensation process. The average particle size of SnO_2 NPs loaded on rGO was estimated to be about 5.0 nm (**Fig. S2c**), almost identical with the dimensional size of SnO_2 on g-C_3N_4 (4.8 nm). During the loading of tin oxides under the solvothermal conditions, the graphene oxide (GO) nanosheets were thermally reduced with the partial removal of oxygen-containing functional groups at the surfaces. As a result, the electrostatic repulsion between the functional groups was weakened and the reduced graphene oxide (rGO) nanosheets became destabilized. To resist the strain, the surfaces of rGO turned to be more folded spontaneously to achieve an equilibrium state with the lowest energy.

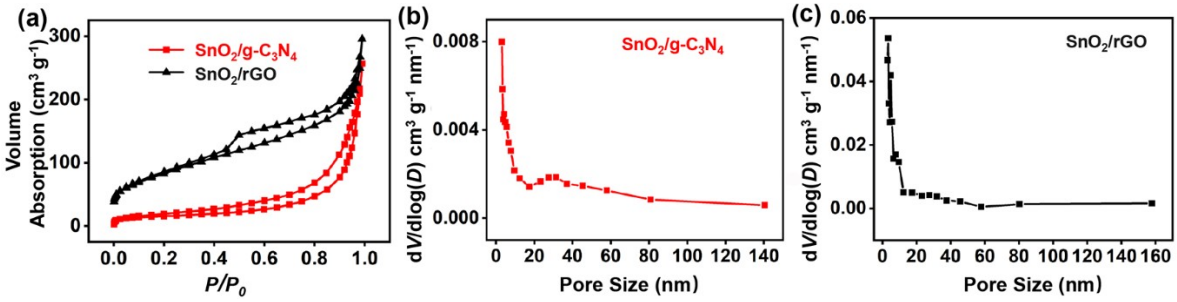

Fig. S3. N_2 adsorption isotherms (a) and corresponding pore size distributions (b-c) of SnO_2/g-C_3N_4 (b) and SnO_2/rGO (c).

N_2 adsorption-desorption curves of the samples were measured at 77 K in a liquid nitrogen bath. SnO_2/rGO showed slightly higher N_2 uptake than SnO_2/g-C_3N_4 (**Fig. S4a**). The BET surface areas were calculated to be 53.26 and 195.97 m^2/g for SnO_2/g-C_3N_4 and SnO_2/rGO, respectively. Correspondingly, the pore size distributions were determined using the Barrett-Joyner-Halenda (BJH) method based on the adsorption branches. As can be seen from **Fig. S4b-c**, the pores of SnO_2/g-C_3N_4 and SnO_2/rGO centered around 6.5 and 3.4 nm, respectively.

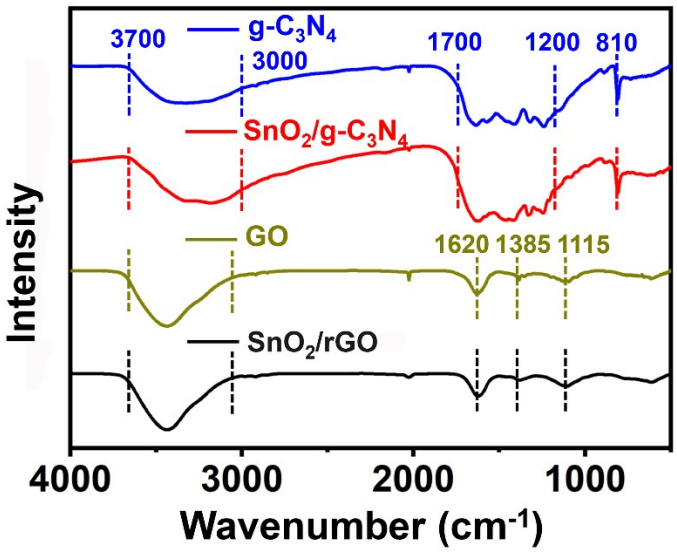

Fig. S4. FTIR spectra of g-C_3N_4, SnO_2/g-C_3N_4, GO, and SnO_2/rGO

For g-C_3N_4 (blue line) and SnO_2/g-C_3N_4 (red line), the broad peak from 3000 cm^{-1} to 3700 cm^{-1} corresponded to the stretching vibration of amine groups or water. [4] The waves occurred between 1200 and 1700 cm^{-1} were ascribed to CN heterocycles' stretching and bending modes.[5] The breathing mode of tri-s-triazine units showed up at about 810 cm^{-1}.[6] Similarly, for GO (olive line) and SnO_2/rGO (black line), the broad peak from 3100 cm^{-1} to 3700 cm^{-1} was typical of the stretching vibration of the absorbed water molecules. The stretching vibration of C-O bond and sp^2 hybridized C=C bond occurred at about 1115 and 1620 cm^{-1}, respectively. The peak located around 1385 cm^{-1} was assigned to the deformation mode of C-O-H.[7] In all, the FTIR spectra showed no obvious differences between the substrates and the corresponding composites loaded with SnO_2 nanoparticles, indicating that the compositions and chemical groups were

well preserved during the hydrothermal synthesis process.

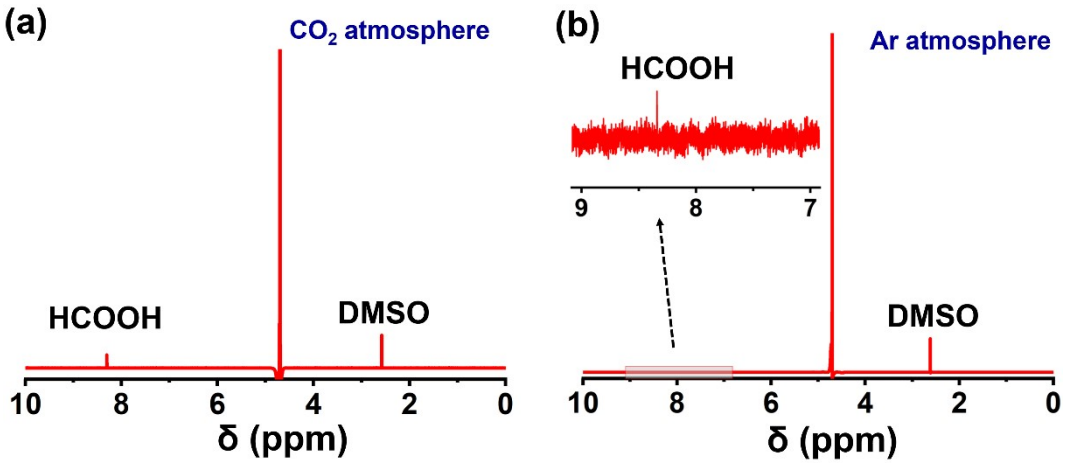

Fig. S5. ^{1}H-NMR spectra of electrolytes after electrolysis at 1.06 V *vs*. RHE for 1 h under the CO_2 (a) and Ar (b) atmospheres over SnO_2/g-C_3N_4, respectively.

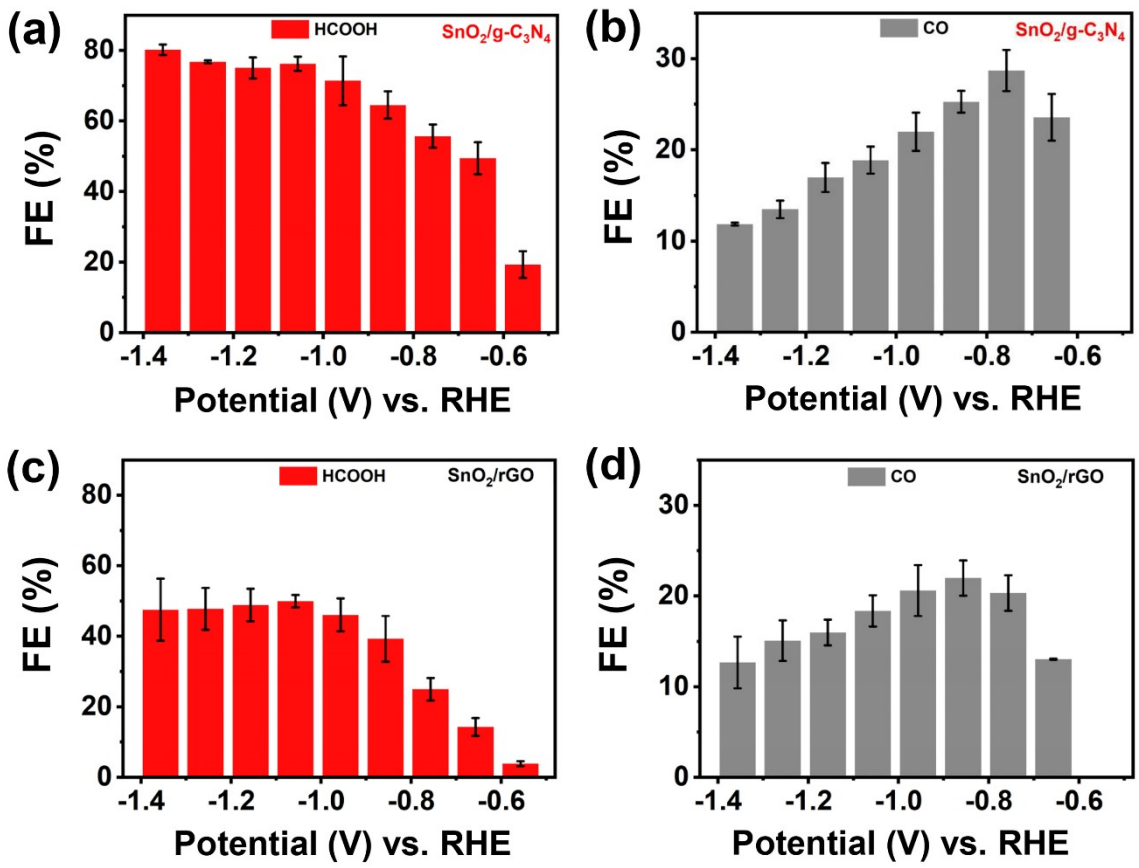

Fig. S6. Faradaic efficiencies of HCOOH (a, c) and CO (b, d) for SnO_2/g-C_3N_4 and SnO_2/rGO at different potentials.

The liquid and gas products during electrolysis were detected by the ^{1}H-NMR (**Fig. S5**) and GC spectra (**Fig. S7**), respectively. The FEs of HCOOH for SnO_2/g-C_3N_4 (19.3-80.2%) electrode were significantly higher than that for SnO_2/rGO (3.9-50.0%) (**Fig. S6a, c**). In contrast, the difference of the CO generating ability of the two catalysts was not that big (**Fig. S6b, d**). Both catalysts exhibited volcano-like trends between CO FEs and the potentials. For SnO_2/g-C_3N_4, the values ranged from 11.8% to 28.7%, whereas for SnO_2/rGO, the values varied from 12.6% to 21.9%. Overall, the former showed slightly higher selectivity toward CO than the latter.

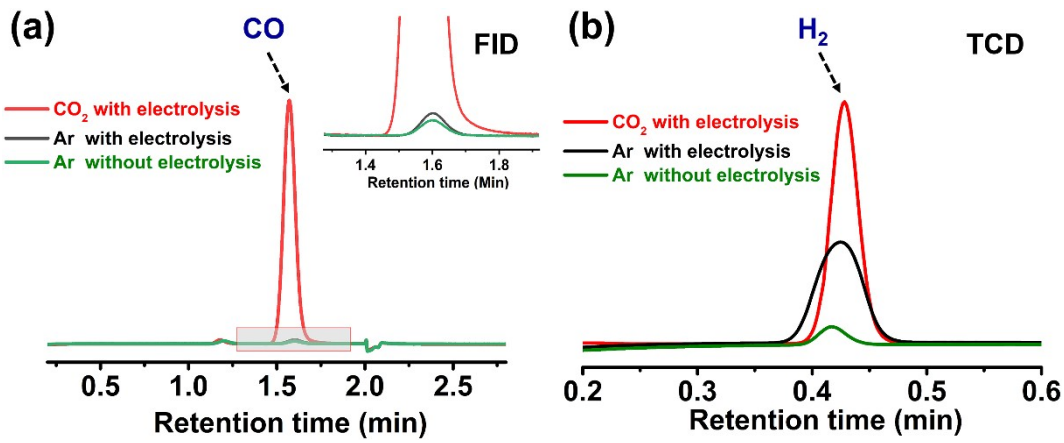

Fig. S7. GC spectra of the gas products of CO and H_2 detected by the FID and TCD after electrolysis at 1.06 V *vs*. RHE for 1 h under the atmosphere of CO_2 or Ar. For comparison, the feeding gas of Ar was directly purged into the GC. It can be observed that trace amounts of CO and H_2 were present in the feeding Ar gas.

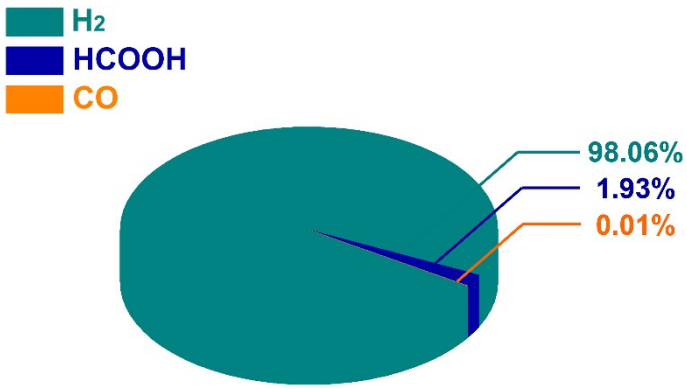

Fig. S8. 3D color pie chart for the faradaic efficiencies of H_2, HCOOH and CO after electrolysis at -1.06 V v*s*. RHE for 1 h under the atmosphere of Ar.

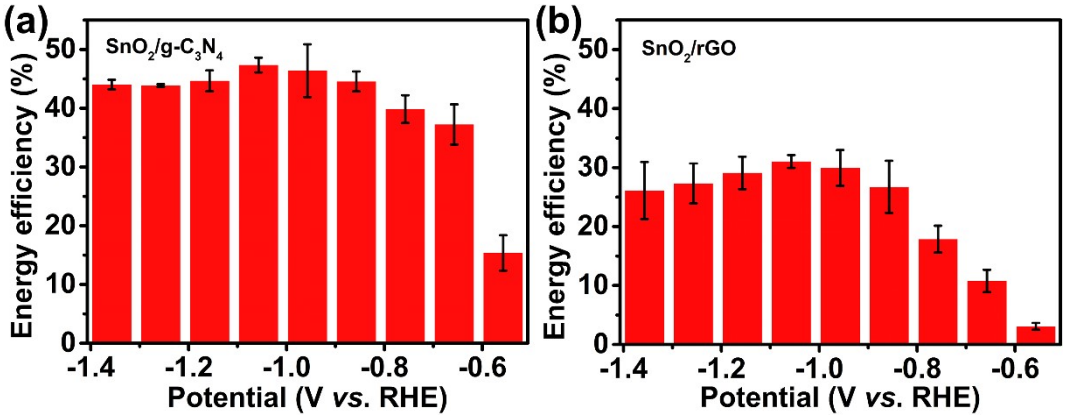

Fig. S9 Potential-dependent energy efficiencies for converting CO_2 into HCOOH over SnO_2/g-C_3N_4 (a) and SnO_2-rGO (b).

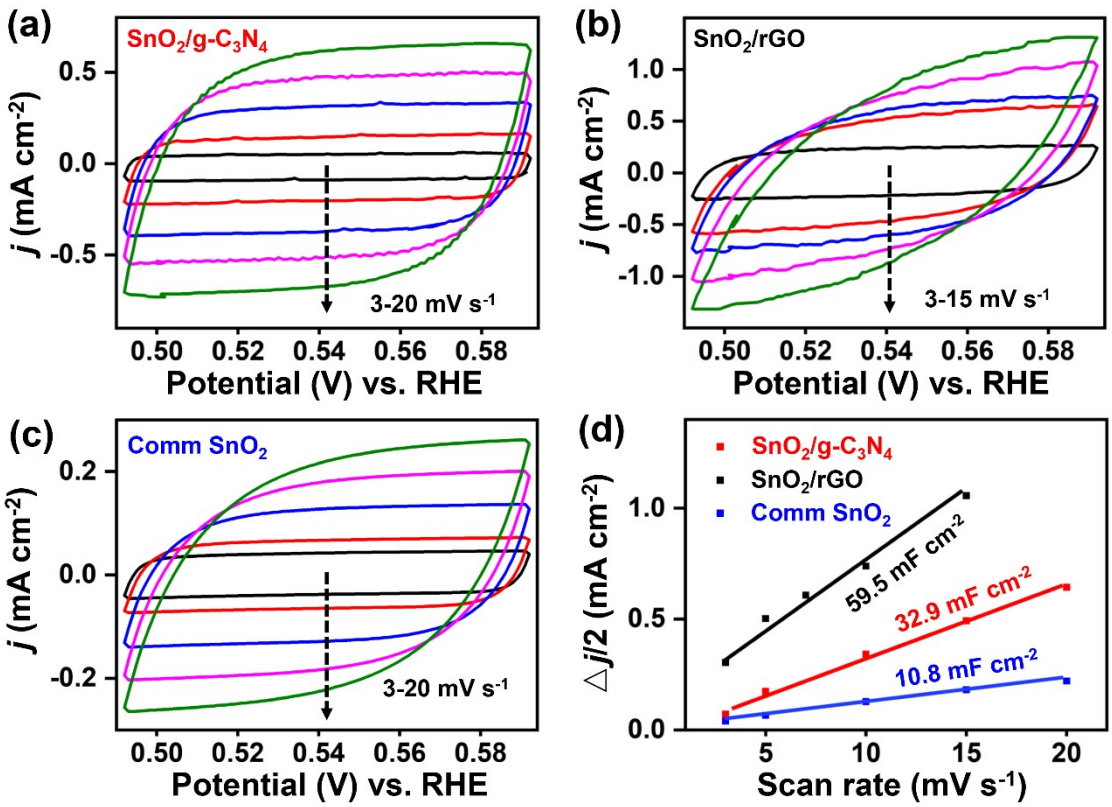

Fig. S10. CV curves obtained with the scan rates from 10 to 50 mV s^{-1} on SnO_2/g-C_3N_4 (a), SnO_2/rGO (b) and commercial SnO_2 (c) and the corresponding double-layer capacitances (d).

The ECSA of SnO_2/g-C_3N_4, SnO_2/rGO and commercial SnO_2 were evaluated based on the double-layer capacitances (C_{dl}) (**Fig. S10**). Obviously, the value of C_{dl} for SnO_2/rGO (59.5 mF cm^{-2}) was almost two and six times that of SnO_2/g-C_3N_4 (32.9 mF cm^{-2}) and commercial SnO_2 (10.8 mF cm^{-2}), respectively. As shown in **Fig. S11**, after normalization to the double-layer capacitance, the partial current densities of C1 products for SnO_2/g-C_3N_4 were higher than those of SnO_2/rGO over the entire potential range. Specifically, the value for SnO_2/g-C_3N_4 (0.29 mA mF^{-1}) is about four times that for SnO_2/rGO (0.07 mA mF^{-1}) at -1.36 V.

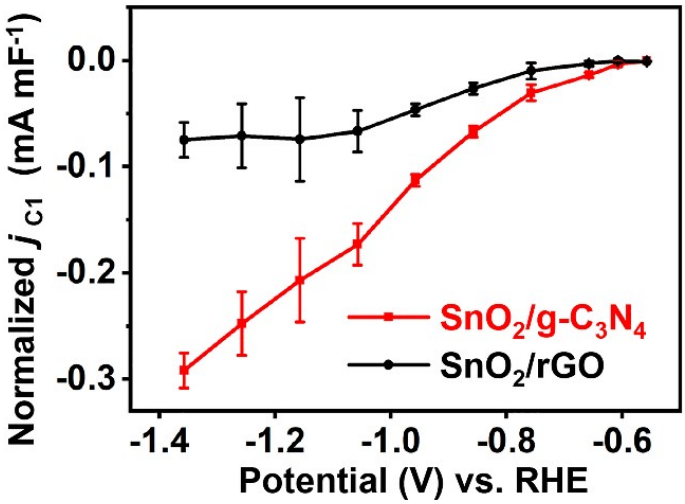

Fig. S11. Normalized C_1 partial current densities for SnO_2/g-C_3N_4 and SnO_2/rGO.

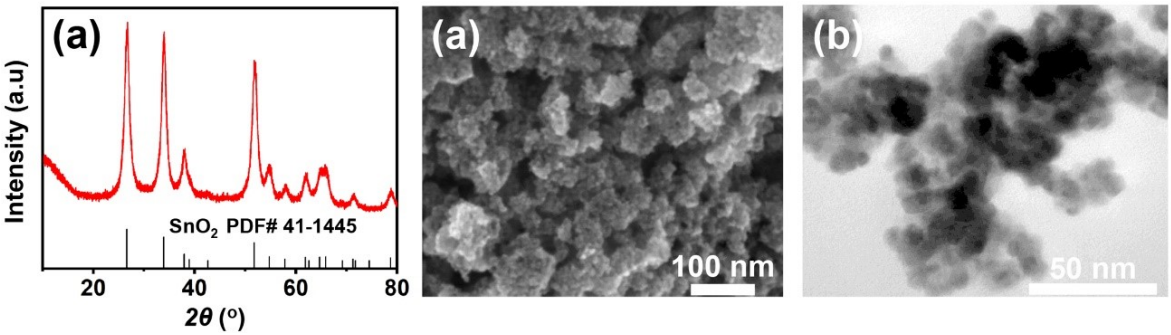

Fig. S12. (a) XRD pattern, (b) SEM and (c) TEM images of commercial SnO_2.

The typical diffraction peaks of commercial SnO_2 match well with the tetragonal SnO_2 (PDF #41-1445) (**Fig. S12 a**). SEM and TEM images indicate the uniformity of the SnO_2 NPs (**Fig. S12 b, c**). The differences in LSV curves taken under Ar and CO_2-saturated 0.1 M $KHCO_3$ solutions suggest that the commercial SnO_2 is also active for CO_2RR (**Fig. S13 a**). Product analysis shows that the FE of HCOOH varies from 13.2% to 71.3%. Meanwhile, the FE of C_1 products increases from 13.2% to 89.1%. The CO_2RR performances of commercial SnO_2 were superior to those of SnO_2/rGO but inferior to SnO_2/g-C_3N_4.

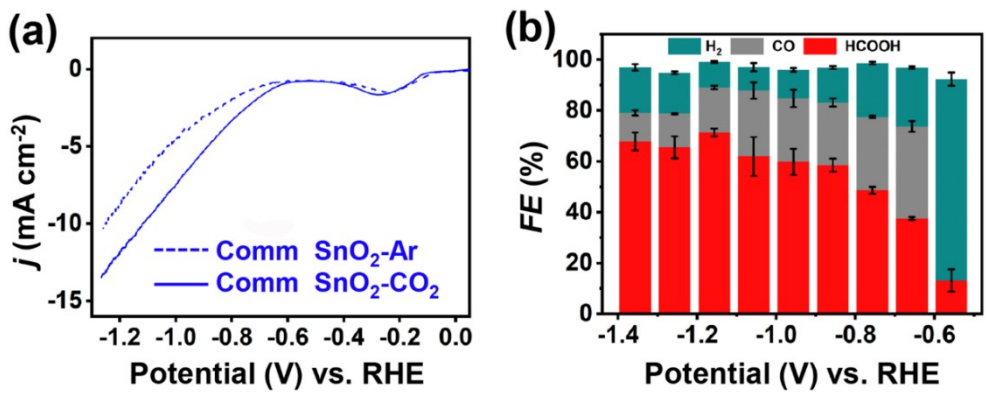

Fig. S13. LSV curves in Ar- and CO_2-saturated 0.1 M $KHCO_3$ (a) and the corresponding FEs of H_2, CO and HCOOH over commercial SnO_2.

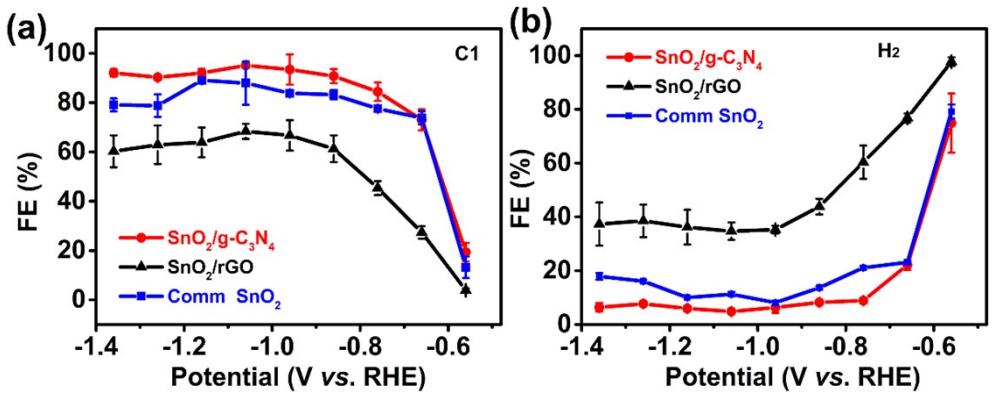

Fig. S14 Faradaic efficiencies of C1 products (a) and H_2 (b) at different potentials over SnO_2/g-C_3N_4, SnO_2/rGO and commercial SnO_2.

The CO_2RR performances of commercial SnO_2 were also investigated (**Fig. S13** and **S14**). The faradaic efficiencies of C1 products and H_2 at different potentials over SnO_2/g-C_3N_4, SnO_2/rGO and commercial SnO_2 were compared in **Fig. S14**. In terms of faradaic efficiencies of C1 products, SnO_2/g-C_3N_4 took obvious advantage over commercial SnO_2 at potentials more negative than -0.66 V. The maximum difference between the two samples reached about 13%. At potentials more positive than -0.66 V, they exhibited similar selectivity for C1 products. Noticeably, both were superior to the sample of SnO_2/rGO in producing C1 products from CO_2RR. The performance distinctions between the three samples further highlighted the importance of the metal oxide-support interaction in improving the catalytic properties.

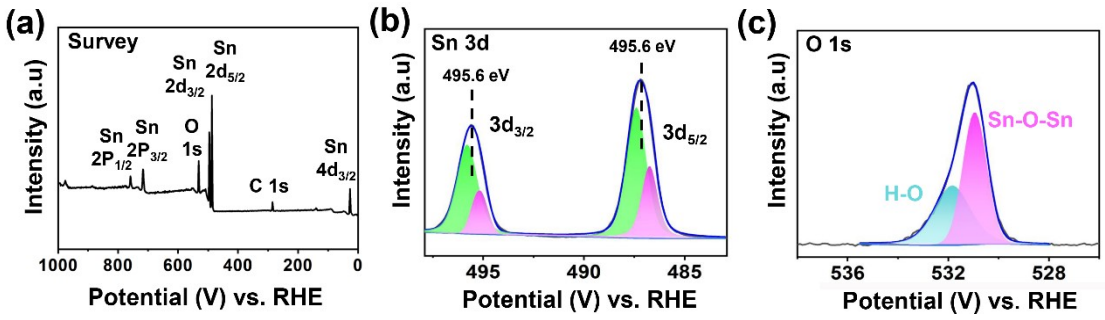

Fig. S15. Survey (a), Sn 3d (b) and O 1s spectra (c) of commercial SnO_2.

The survey XPS results indicate the presence of Sn and O in commercial SnO_2. The high-resolution Sn 3d XPS spectra show the $Sn_{3/2}$ and $Sn_{5/2}$ peak are located at 495.6 and 487.2 eV, respectively. Noticeably, the bivalent Sn^{2+} takes up 77% of the total surface Sn species. By careful comparison, we found that the FEs for HCOOH or C_1 product showed an increasing trend with the decrease of the binding energy of Sn $3d_{3/2}$ from 496.0 to 495.6 to 495.0 eV, implying that the chemical state of Sn species in the catalysts had significant impact on the CO_2RR performances.

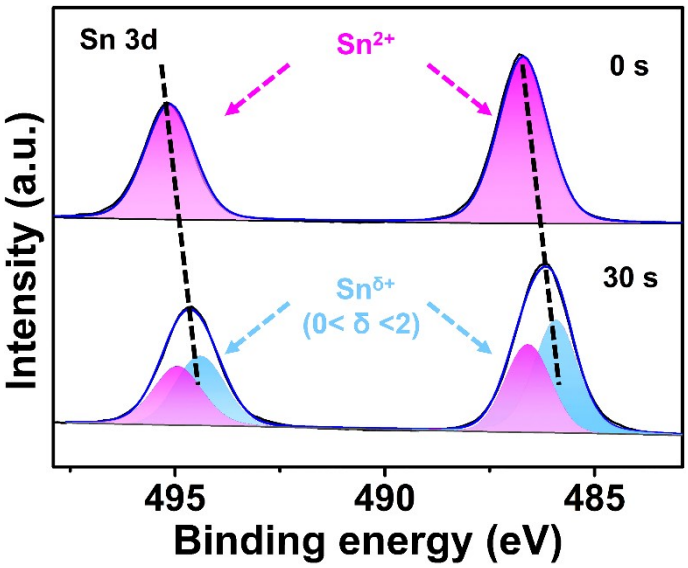

Fig. S16. Regular core-level Sn 3d XPS and depth profiles with 30 s Ar sputtering for SnO_2/g-C_3N_4 after reaction.

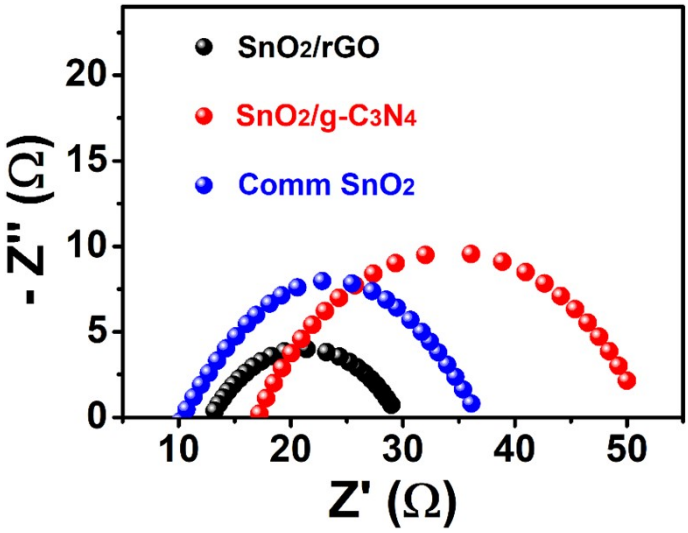

Fig. S17. Nyquist plots of SnO_2/g-C_3N_4, SnO_2/rGO and commercial SnO_2 at -1.06 V.

As can be seen from the Nyquist plots in **Fig. S17**, the charge transfer resistance increased from SnO_2/rGO to commercial SnO_2 and to SnO_2/g-C_3N_4. Noticeably, the value of the commercial SnO_2 lied in between that of SnO_2/rGO and SnO_2/g-C_3N_4. The smaller resistance for SnO_2/rGO compared with SnO_2/g-C_3N_4 might originate from the inherently higher electrical conductivity of rGO. Even though, SnO_2/g-C_3N_4 still delivered a higher partial current density of C_1 products, further confirming the intrinsic structural superiority of SnO_2/g-C_3N_4 in CO_2RR.

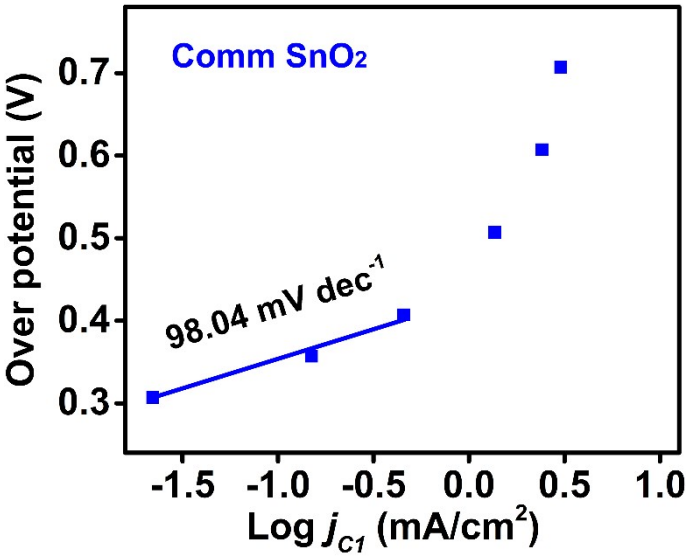

Fig. S18. Tafel plot for the commercial SnO_2.

Table S1. Comparison of CO_2RR properties of Sn-based catalysts for C_1 product.

Catalyst	Electrolyte	Potential (V vs. RHE)	FE_{C1} (%)	Stability (h)	Ref.
Sn/CP-UPED	0.1 M $KHCO_3$	-1.16	92	10	8
SnO_2 QWs	0.1 M $KHCO_3$	-1.05	90	7	9
Sn-CF1000	0.1 M $KHCO_3$	-0.80	91	24	10
heat-treated Sn dendrite	0.1 M $KHCO_3$	-1.40	85	18	11
Mn-doped SnO_2	0.1 M $KHCO_3$	-1.05	91	7.6	12
mSnO_2 NTs-350	0.5 M $KHCO_3$	-1.20	97	12	13
SnO_2@N-rGO	0.5 M $NaHCO_3$	-0.80	89	20	14
N-Sn(s)	0.1 M $KHCO_3$	-0.70	96	20	15
Vo-rich SnO_2	0.5 M $KHCO_3$	-1.10	92	30	16
WIT SnO_2	0.1 M $KHCO_3$	-1.00	93	14	17
SnO_2 porous nanowire	0.1 M $KHCO_3$	-1.00	87	15	18
m-SnO_2	0.1 M $KHCO_3$	-1.15	80	16	19
SnO_2-nanoflakes	0.1 M $KHCO_3$	-1.00	91	10	20
Single-atom $Sn^{\delta+}$ on N-doped graphene	0.25 M $KHCO_3$	-0.96	88	200	21
Bi-SnO/Cu foam	0.1 M $KHCO_3$	-1.10	94	30	22
SnO_2/g-C_3N_4	**0.1 M $KHCO_3$**	**-1.06**	**95**	**70**	**This work**

References

1. Y. Dai, C. Li, Y. Shen, T. Lim, J. Xu, Y. Li, H. Niemantsverdriet, F. Besenbacher, N. Lock and R. Su, Nat. Commun., 2018, **9**, 60.
2. J. Xie, X. Sun, N. Zhang, K. Xu, M. Zhou and Y. Xie, Nano Energy, 2013, **2**, 65-74.
3. X. Shi, M. Fujitsuka, S. Kim and T. Majima, Small, 2018, **14**, 1703277.
4. L. Zhang, F. Mao, L. R. Zheng, H. F. Wang, X. H. Yang and H. G. Yang, ACS Catal., 2018, **8**, 11035-11041.
5. N. Meng, J. Ren, Y. Liu, Y. Huang, T. Petit and B. Zhang, Energy Environ. Sci., 2018, **11**, 566-571.
6. D. T. Whipple and P. J. A. Kenis, J. Phys. Chem. Lett., 2010, **1**, 3451-3458.
7. H. Shen, X. Zhao, L. Duan, R. Liu, H. Wu, T. Hou, X. Jiang and H. Gao, Appl. Surf. Sci., 2017, **391**, 627-634.
8. X. An, S. Li, A. Yoshida, Z. Wang, X. Hao, A. Abudula and G. Guan, ACS Sustainable Chem. Eng., 2019, **7**, 9360-9368.
9. S. Liu, J. Xiao, X. F. Lu, J. Wang, X. Wang and X. W. Lou, Angew. Chem. Int. Ed., 2019, **58**, 8499-8503.
10. Y. Zhao, J. Liang, C. Wang, J. Ma and G. G. Wallace, Adv. Energy Mater., 2018, **8**, 1702524.
11. D. H. Won, C. H. Choi, J. Chung, M. W. Chung, E.-H. Kim and S. I. Woo, ChemSusChem, 2015, **8**, 3092-3098.
12. Y. Wei, J. Liu, F. Cheng and J. Chen, J. Mater. Chem. A, 2019, **7**, 19651-19656.
13. F. Wei, T. Wang, X. Jiang, Y. Ai, A. Cui, J. Cui, J. Fu, J. Cheng, L. Lei, Y. Hou and S. Liu, *Adv. Funct. Mater.*, 2020, **30**, 2002092.
14. B. Zhang, Z. Guo, Z. Zuo, W. Pan and J. Zhang, Appl. Catal. B-Environ., 2018, **239**, 441-449.
15. H. Cheng, S. Liu, J. Zhang, T. Zhou, N. Zhang, X.-s. Zheng, W. Chu, Z. Hu, C. Wu and Y. Xie, Nano Lett., 2020, **20**, 6097-6103.
16. H. He, K. Liu, K. Liang, A. Mustapha, Z. Wang, L. Wu, C. Yang, L. Deng, S. Guo and Y.-N. Liu, J. Catal., 2020, **385**, 246-254.
17. L. Fan, Z. Xia, M. Xu, Y. Lu and Z. Li, Adv. Funct. Mater., 2018, **28**, 1706289.
18. B. Kumar, V. Atla, J. P. Brian, S. Kumari, T. Q. Nguyen, M. Sunkara and J. M. Spurgeon, Angew. Chem. Int. Ed., 2017, **56**, 3645-3649.
19. R. Lin, X. Ma, W.-C. Cheong, C. Zhang, W. Zhu, J. Pei, K. Zhang, B. Wang, S. Liang, Y. Liu, Z. Zhuang, R. Yu, H. Xiao, J. Li, D. Wang, Q. Peng, C. Chen and Y. Li, Nano Res., 2019, **12**, 2866-2871.
20. X. Zhang, Z. Chen, K. Mou, M. Jiao, X. Zhang and L. Liu, Nanoscale, 2019, **11**, 18715-18722.
21. X. Zu, X. Li, W. Liu, Y. Sun, J. Xu, T. Yao, W. Yan, S. Gao, C. Wang, S. Wei and Y. Xie, Adv. Mater., 2019, **31**, 1808135.
22. X. An, S. Li, A. Yoshida, T. Yu, Z. Wang, X. Hao, A. Abudula and G. Guan, ACS Appl. Mater. Interfaces, 2019, **11**, 42114-42122.